

Mesoscale investigations of fluid-solid interaction: Liquid slip flow in a parallel-plate microchannel

Zi Li^{1, 2*}, Jiawei Li², Guanxi Yan², Sergio Galindo-Torres¹, Alexander Scheuermann², and Ling Li¹

¹ School of Engineering, Westlake University, Hangzhou, China.

² School of Civil Engineering, The University of Queensland, Brisbane, Australia.

* Corresponding author. Email address: lizi@westlake.edu.cn (Zi Li).

Abstract

Liquid slip flow with the Knudsen number (Kn) of 0.001–0.1 plays a dominated role in microfluidic devices and tight porous media. Its physical origin can be attributed to the intermolecular fluid-solid (F-S) interaction force, which needs to be theoretically formulated. To this end, we proposed the continuous exponentially and power law decaying force functions between fluid particles and flat walls in the framework of mesoscopic lattice Boltzmann model (LBM). It is the first time to derive the analytical solutions of density and velocity profiles, slip length and permeability ratio, which are directly related to the mesoscale F-S interaction parameters and the gap size of flow channel, for the liquid slip flow between two confined parallel plates. The analytical solutions agreed well with the LBM solutions. Reasonable ranges of the F-S interaction parameters were suggested based on the observed range of density ratio (film fluid to bulk fluid) and the increasing permeability ratio with the narrowing gap size. The analytical solutions were also applied to a benchmark slip flow experiment of [Tretheway & Meinhart \(Phys. Fluids 14, 2002, L9\)](#). The continuous F-S interaction force curves with two free parameters were calibrated based on the velocity profile obtained from the validated LBM model of [Li *et al.* \(Phys. Rev. E 98, 2018a, 052803\)](#). The mesoscopic LBM model based on the proposed F-S interaction force functions is capable to elucidate the physical mechanisms of the liquid slip flow.

Key words: slip flow, fluid-solid interaction force, lattice Boltzmann model, analytical solution

1. Introduction

The phenomenon of fluid slip has always been recognized in the continuum fluid dynamics. Due to the slip amount as little as a slip length of 1–100 nm ([Bocquet & Charlaix, 2010](#)), the no-slip condition works well for macroscale flows, but the slip flow will play a dominated role in microfluidic devices. This paper will focus on the liquid flow in the slip regime for the Knudsen number (Kn) in the range of 0.001–0.1 ([Roy *et al.*, 2003](#)). It has been revealed by measurements of the flow rate in thin capillaries ([Schnell, 1956](#); [Churaev *et al.*, 1984](#)) and the velocity profile in microchannel flows ([Tretheway & Meinhart, 2002](#); [Joseph & Tabeling, 2005](#)). The adsorbed water layer ([Liu *et al.*, 2006](#)) and the lower-than-expected water flow ([Cheng *et al.*, 2017](#)) can also be observed in low permeability reservoirs. Therefore the fluid slip (damping) should be accounted for with care in estimating the transport properties of a liquid in tight porous media ([Afsharpoor & Javadpour, 2016](#)).

[Ruckenstein & Rajora \(1983\)](#) proposed that the fluid slip occurred over a gap (rather than directly on solid walls) which was generated by a release of entrained or soluble gas. [Derjaguin & Churaev \(1987\)](#) attributed the slip flow to depleted water region or vapour layer. Such arguments were supported by

the microbubbles observed near hydrophobic surfaces (Ishida *et al.*, 2000), and flow models considering the thickness of depleted water region or air gap were established (Tretheway & Meinhardt, 2004). Martini *et al.* (2008) attributed the liquid slip to the localized liquid atoms hopping at low levels of forcing, and the instantaneous motion of all liquid atoms at high levels of forcing, respectively. Nevertheless, the physical mechanism of fluid slip (damping) is still poorly understood.

Richardson (1973) argued that, when the intermolecular attraction between liquid molecules and solid walls became much weaker than that between liquid molecules themselves, the liquid could not fully wet the solid, and thus slip flow occurred over the solid surface. Compared with wettability, the interaction force between liquid molecules and solid surface is a more intrinsic index of hydrophobicity of a solid surface. Because it recognizes the existence of adsorbed liquid layer leading to negative slip lengths (Davis & Lauga, 2009), and the fact that the liquid can slip on hydrophilic surfaces (Ho *et al.*, 2011). The microscopic molecular dynamics (MD) simulation (Huang *et al.*, 2008; Wu *et al.*, 2017) and the mesoscopic lattice Boltzmann method (LBM) (Zhang & Kwok, 2004; Zhang *et al.*, 2004; Benzi *et al.*, 2006a, 2006b; Harting *et al.*, 2006; Kunert & Harting, 2008; Li *et al.*, 2018a) explored the relationship between amount of the slip and strength of the fluid-solid (F-S) interaction.

The F-S interaction force is responsible for an apparent hydrophobic slip, and hence can be quantified by the difference between hydrodynamic forces on the hydrophilic surface as a no-slip boundary and on the hydrophobic surface with a slip flow (Baudry *et al.*, 2001; Craig *et al.*, 2001). Moreover, it was recognized as an apparent extra attraction by Vinogradova (1998, 1999) and determined by the total hydrodynamic force subtracting van der Waals attraction, hydrophobic attraction and Reynolds drag. The F-S interaction force is a few orders of magnitude greater than the van der Waals attraction, and decays with the distance between liquid molecules and solid walls, but still cannot be expressed by a theoretical formula. The exponentially and power law decaying functions of hydrophobic attraction force between solid surfaces (Vinogradova, 1998, 1999) may provide a useful analogy to the F-S interaction force.

The F-S interaction was quantified in the MD simulation using the Lennard-Jones potential, with tunable interaction energies and molecular diameters to recover the contact angle. The LBM method employed an exponentially decaying force function or an interaction potential within a single lattice layer to model the F-S interaction. Assuming a no-slip boundary (no true slip on solid surface), the interaction strength (and the decay length) was adjustable to result in the apparent fluid slip (damping) behaviour. Among them, the continuous force function was established between fluid particles and flat walls and at the particle level, and the latter force function was able to investigate the liquid slip flow in porous media. Some other LBM models studied the fluid slip on solid surface by combining the bounce-back and specular reflection boundary conditions (Succi, 2002; Zhu *et al.*, 2005), by linking the LBM relaxation time with Kn (Tang *et al.*, 2004, 2005) and by the use of empirical constitutive relationships between slip velocity and Kn (Sbragaglia & Succi, 2005; Benzi *et al.*, 2006c). The mesoscopic LBM approach is advantageous in that, it takes into account the physics of F-S interaction, which is impossible in the continuum fluid dynamics. Also, it allows the simulation of slip flow experiments on microfluidic devices and microporous media, with acceptable computational costs compared with the microscopic MD simulation.

Therefore, this study takes advantage of the LBM model framework to investigate the liquid slip flow between two confined parallel plates. By analogizing the hydrophobic attraction force between solid surfaces (Vinogradova, 1998, 1999), the exponentially and power law decaying force functions between fluid particles and flat walls are proposed for the physics of fluid behaviours near solid surface. The details of the LBM model and the proposed continuous force functions are presented in the next section. The analytical solutions for density and velocity profiles, slip length and permeability ratio based on the two continuous force functions are derived in §3. As presented in §4, the obtained analytical solutions are strictly consistent with the numerical solutions of an advanced LBM scheme, and some useful implications in the engineering context are provided. An application of the analytical solutions to a benchmark slip flow experiment is also carried out. Finally, we make some concluding remarks in the last section.

2. Fluid-solid interaction in the lattice Boltzmann model

2.1. Lattice Boltzmann model framework

The LBM model based on the mesoscopic kinetic theory has been widely used for simulations of immiscible two-phase flow (Li *et al.*, 2018b, 2019) and liquid slip flow. Here the intermolecular interaction between liquid molecules themselves is assumed to be negligible compared with the F-S interaction, because the net effect of attraction forces from the neighbouring liquid molecules can be almost offset for a liquid molecule in the interior of bulk fluid. The thermodynamically stable bulk fluid is described by the single-phase LBM model. The particle distribution functions (f_k) for the k -th discrete velocity direction obeys the Bhatnagar-Gross-Krook (BGK) lattice Boltzmann equation (Succi, 2001)

$$f_k(\mathbf{x} + \mathbf{e}_k \Delta t, t + \Delta t) - f_k(\mathbf{x}, t) = \frac{\Delta t}{\tau} [f_k^{\text{eq}}(\mathbf{x}, t) - f_k(\mathbf{x}, t)], \quad (2.1)$$

where, \mathbf{x} , t are position and time, respectively; Δt the time step which is always given by $\Delta t = 1$ time step (ts); \mathbf{e}_k the discrete velocity that is referred to in (Li *et al.*, 2018a) for D_2Q_9 (nine velocities in two-dimensional space) and D_3Q_{19} (nineteen velocities in three-dimensional space) LBMs; $f_k^{\text{eq}}(\mathbf{x}, t)$ the Maxwell-Boltzmann equilibrium distribution function as formulated in (Li *et al.*, 2018a). The relaxation time (τ) is related to the kinematic viscosity (ν) by $\nu = c_s^2 \Delta t (\tau / \Delta t - 0.5)$ in order to recover the macroscopic Navier-Stokes (NS) equation. The sound speed (c_s) is taken as $c_s^2 = 1/3$. The left-hand and right-hand sides of (2.1) are the streaming process passing the particle distribution to the neighbouring nodes, and the BGK collision operator partially relaxing the particle distribution to the equilibrium distribution, respectively.

The explicit force scheme (EFS) is utilized to quantify the momentum transfer when the external body force (\mathbf{F}) is involved. The forcing term (φ_k) accounting for changes in the distribution function and the transformation function (h_k) are defined as (Porter *et al.*, 2012; Li *et al.*, 2018a)

$$\varphi_k(\mathbf{x}, t) = \frac{\mathbf{F} \cdot (\mathbf{e}_k - \mathbf{u}^{\text{eq}})}{\rho c_s^2} f_k^{\text{eq}}(\mathbf{x}, t); \quad h_k(\mathbf{x}, t) = f_k(\mathbf{x}, t) - \frac{\Delta t}{2} \varphi_k(\mathbf{x}, t), \quad (2.2)$$

where, ρ is the macroscopic fluid density, and \mathbf{u}^{eq} the equilibrium velocity equal to the macroscopic flow velocity (\mathbf{u}). By directly incorporating φ_k into the lattice Boltzmann equation in (2.1) with the

collision operator unchanged, and applying h_k to the resulting implicit formula, the following explicit expression of the new particle distribution function (h_k) is yielded

$$h_k(\mathbf{x} + \mathbf{e}_k \Delta t, t + \Delta t) - h_k(\mathbf{x}, t) = \frac{1}{\tau} \left[f_k^{\text{eq}}(\mathbf{x}, t) - h_k(\mathbf{x}, t) - \frac{\Delta t}{2} \varphi_k(\mathbf{x}, t) \right] + \Delta t \varphi_k(\mathbf{x}, t). \quad (2.3)$$

Then the fluid density (ρ) and the flow velocity (\mathbf{u}) can be obtained by

$$\rho = \sum_k h_k; \mathbf{u} = \frac{1}{\rho} \left(\sum_k h_k \mathbf{e}_k + \frac{\Delta t}{2} \mathbf{F} \right). \quad (2.4)$$

When the equation of state of ideal gas is used, the macroscopic fluid pressure (p^*) is given by

$$p^* = c_s^2 \rho. \quad (2.5)$$

The EFS-LBM scheme can inhibit the undesirable spurious velocities and the dependence of numerical results on the relaxation time to a great extent. The LBM simulation of the steady-state flow runs until reaching the equilibrium criterion for flow velocity.

2.2. Fluid-solid interaction force

Combined with the applied bounce-back boundary condition (Succi, 2001) admitting no true slip on solid surface, the F-S interaction force, as the focus of our research, is responsible for an apparent fluid slip. Although a theoretical formulation of the F-S interaction force remains unavailable, it can be established by an analogy to the hydrophobic attraction force between solid surfaces. Recognizing the nature of F-S interaction force at the particle level (Li *et al.*, 2018a) and decaying like an exponential function (EXF) or a power law function (PLF) (Vinogradova, 1998, 1999), the F-S interaction force between fluid particles and flat walls can be obtained by integrating the local forces over the surface of the solid wall, and will maintain the form of EXF or PLF functions. Hence, in a confined parallel-plate microchannel as depicted in figure 1, the individual interaction force (f_s) between fluid particles and each wall can be proposed by

$$f_s(y) = -\rho(y) g_s \exp\left(-\frac{y}{\eta}\right), \quad (2.6a)$$

$$f_s(y) = -\frac{\rho(y) g_s}{y^n}, \quad (2.6b)$$

where, y is the spanwise position of fluid particles in the given coordinate system, g_s the interaction strength determining the magnitude of interaction force, and η , n the decay length and the decay rate, respectively, controlling the decaying behaviour of the two force curves. Given that the gap between two parallel plates is very narrow, the effect of the interaction force exerted by the other wall should be included. So the net interaction force (F_s) from the two flat walls with a gap size of $2R$ can be expressed by

$$F_s(y) = -\rho(y) g_s \left[\exp\left(-\frac{y}{\eta}\right) - \exp\left(-\frac{2R-y}{\eta}\right) \right], \quad (2.7a)$$

$$F_s(y) = -\rho(y) g_s \left[\frac{1}{y^n} - \frac{1}{(2R-y)^n} \right]. \quad (2.7b)$$

The interaction force is applied to the fluid particles, and so it is related to the number density of fluid particles. In this way, the interaction force will change the fluid density and dynamic viscosity near the solid surface. The continuous EXF and PLF force functions in (2.7a, b) allow the simulation of

density and velocity profiles near solid surface. Moreover, the excessive pressure due to the F-S interaction potential plus the ideal gas pressure contributes to the macroscopic fluid pressure (p), as formulated by (Benzi *et al.*, 2006a, 2006b)

$$p = c_s^2 \rho + \int_0^y F_s(s) ds. \quad (2.8)$$

Substituting (2.7a, b) into (2.8) gives the explicit formulations of macroscopic fluid pressure for EXF and PLF force functions, respectively, as the following

$$p(y) = c_s^2 \rho(y) - g_s \int_0^y \rho(s) \left[\exp\left(-\frac{s}{\eta}\right) - \exp\left(-\frac{2R-s}{\eta}\right) \right] ds, \quad (2.9a)$$

$$p(y) = c_s^2 \rho(y) - g_s \int_0^y \rho(s) \left[\frac{1}{s^n} - \frac{1}{(2R-s)^n} \right] ds. \quad (2.9b)$$

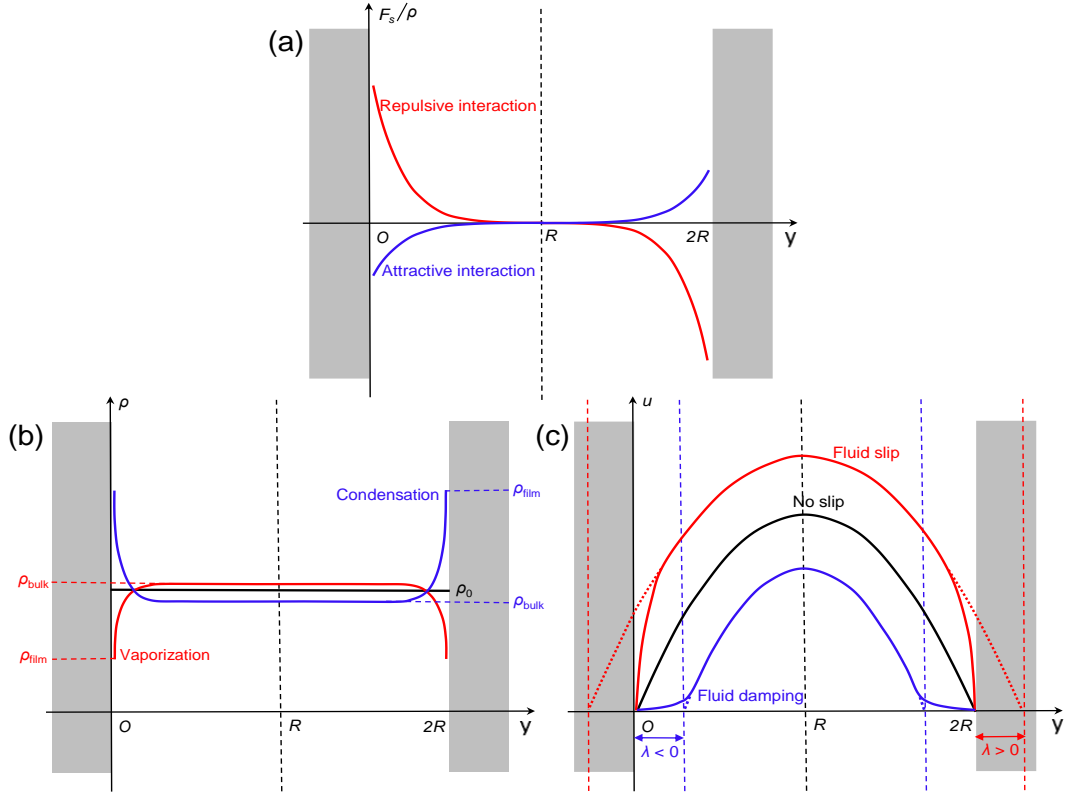


FIGURE. 1. Diagram of a confined parallel-plate microchannel with a gap size of $2R$ and an upward flow. The microchannel may be two-dimensional (with two straight walls) or three dimensional (with two flat surfaces). (a) The force curves of the net interaction from the two flat walls for the repulsive and attractive F-S interactions. (b) The densities profiles $\rho(y)$ and the densities of film liquid (ρ_{film}) and bulk liquid (ρ_{bulk}), when the vaporization and condensation effects take place. (c) The velocity profiles $u(y)$ and the slip lengths (λ) for different flow behaviours (fluid slip, fluid damping and no slip).

The decaying curves of the two force functions are portrayed in figure (1a). The magnitude of net interaction force reaches the maximum near solid surface, and decays to zero in the middle of the channel, where the individual interaction forces from the two flat walls are completely offset. The net (and individual) F-S interaction force is repulsive (attractive) for $g_s > 0$ ($g_s < 0$), and decays faster for smaller η (larger n). Both larger $|g_s|$ and longer interaction distance (slower decaying process) indicate stronger F-S interactions. However, we should avoid an extreme case, where the parallel-plate microchannel is very confined (relative to the given individual decaying interaction force), and accordingly the net interaction force becomes very weak even for the strong individual interaction

force. It will lead to a physically inconsistent result that, the effect of net F-S interaction on the macroscale flow properties decreases with the narrowed gap between two flat walls, and our mesoscopic LBM model will fail. This extreme case is characterized by a high Kn ($Kn > 0.1$), where the collision between liquid molecules themselves becomes much less frequent, and the NS equation cannot describe the macroscopic flow property adequately. In this case, the intermolecular interaction between liquid molecules themselves and the F-S interaction can be better described by the Lennard-Jones potential in the microscopic MD simulation.

2.3. Fluid-solid interaction effect on flow properties

The solid walls tend to exert the repulsive (or attractive) force to the fluid particles at the mesoscale due to their physicochemical property. The liquid molecules, as a result, are expelled from (or gather near) solid surfaces, and the liquid density in a very thin layer close to solid surfaces becomes a bit smaller (or larger) than the bulk liquid density, which is referred to as the vaporization (or condensation) effect (see figure 1(b)). The density difference between the film liquid density and the free liquid density has been confirmed experimentally on bound water adsorbed on various surfaces (Ewing & Spurway, 1930; Anderson & Low, 1957; Martin, 1962; Olodovskii, 1967, 1981; Kulasinski, 2016). The bound water density was also observed to increase with its reduced content (film thickness), showing that the film liquid density rises as the liquid layer becomes thinner (closer to the solid surface) (see figure 1(b)). The density ratio of film liquid to bulk liquid is defined as below

$$\rho_{ra} = \frac{\rho_{film}}{\rho_{bulk}}. \quad (2.10)$$

In our analytical solutions obtained in the next section, the fluid densities at $y_1 = 1$ lattice unit (lu) (closest to solid surface in the lattice grid system) and $y_2 = R$ are used to represent the film and bulk fluid densities, respectively, that is, $\rho_{film} = \rho(1)$ and $\rho_{bulk} = \rho(R)$. The ranges of density ratio under various experimental conditions are summarized in table 1.

TABLE 1. Density ratio range observed in various experimental investigations.

Reference	Liquid	Solid material	ρ_{ra} range
(Ewing & Spurway, 1930)	Water	Silica gel	0.54–1.03
(Anderson & Low, 1957)	Water	Bentonite clay	0.97–0.98
(Martin, 1962)	Water	Kaolinite	0.99–1.68
		Montmorillonite	1.02–1.41
(Olodovskii, 1967)	Water	Glukhovtes kaolin	1.1–1.5
		Cherkassy bentonite	1.1–1.8
(Olodovskii, 1981)	Water	Natural kaolinite	0.98–1.22
		Natural montmorillonite	1.06–1.15
(Kulasinski, 2016)	Water	Cellulose	0.2–1.3

The vaporized (condensed) film liquid leads to a decrease (increase) of shear viscosity near solid surface and the resulting flow becomes faster (slower) near solid surface and in the bulk fluid than that under the no-slip condition, which is the so-called apparent fluid slip (damping) behaviour (see figure 1(c)). It is consistent with the argument (Ruckenstein & Rajora, 1983; Derjaguin & Churaev, 1987) that, the slip slow is due to (and occurs on) depleted water region or vapour layer near the hydrophobic surface. Under the no-slip condition, the velocity (u^*) profile between two parallel plates is a Poiseuille-type curve (see figure 1(c)), as given by

$$u^*(y) = \frac{g}{2\nu} y(2R - y), \quad (2.11)$$

where, g is the acceleration of the external body force to drive the fluid flow. In the presence of repulsive (attractive) F-S interaction, the near-wall velocity still vanishes at the wall, but the bulk velocity (u) profile considering the apparent fluid slip (damping) behaviour can be approximated by introducing a positive (negative) slip length (λ) (see figure 1(c)), as follows

$$u(y) = \frac{g}{2\nu} (y + \lambda)(2R + \lambda - y). \quad (2.12)$$

It is still a Poiseuille-type curve but extrapolates to zero outside (inside) the solid wall. Thus (2.12) overestimates (underestimates) the near-wall velocity and the volumetric flux. The slip length is the distance between the fictitious solid wall where the bulk velocity extrapolates to zero and the real solid wall, quantifying the amount of apparent fluid slip (damping). The F-S interaction effect on the bulk flow property is equivalent to that, the gap between two flat walls increases to $(2R + 2\lambda)$. The slip lengths of typical and engineered hydrophobic surfaces range from 1–100 nanometres (Bocquet & Charlaix, 2010) to around 1 micrometre (μm) (Tretheway & Meinhart, 2002). The kinematic viscosity of bulk fluid is, however, not affected by the F-S interaction (Li *et al.*, 2018a). Thus, the change of dynamic viscosity is due to the change of density induced by the F-S interaction. In this way, the F-S interaction can be coupled with the dynamic viscosity and the resulting slip flow.

The permeability ratio (k_{ra}) (also referred to as flow enhancement ratio), as a ratio of the flux (Q_{slip}) in the slip flow to the flux ($Q_{\text{no-slip}}$) in the no-slip flow, is defined to describe the change in the flow property as below

$$k_{ra} = \frac{Q_{\text{slip}}}{Q_{\text{no-slip}}}. \quad (2.13)$$

where, $Q_{\text{no-slip}}$ and Q_{slip} may be volumetric flux or mass flux. The flow enhancement ratio of thin channels varies from 1.05 (Schnell, 1956) to 1.30 (Churaev *et al.*, 1984). For the fluid slip (damping) behaviour where $g_s > 0$ ($g_s < 0$), the fictitious no-slip plane lies within the solid (fluid), resulting in a positive (negative) slip length, such as, $\lambda > 0$ ($\lambda < 0$) (see figure 1(c)); and the permeability of the microchannel increases (decreases) with $k_{ra} > 1$ ($k_{ra} < 1$).

3. Derivations of analytical solutions

In the hydrodynamic limit of a small Kn ($\text{Kn} < 0.1$), the lattice Boltzmann equation in (2.1) can recover the NS equation in the continuum fluid dynamics using the Chapman-Enskog expansion (Succi, 2001; Benzi *et al.*, 2006a, 2006b), namely,

$$\partial_t(\rho u_i) + (u_j \partial_j)(\rho u_i) = -\partial_i p + F_i + \nu \partial_j(\rho \partial_j u_i + \rho \partial_i u_j), \quad (3.1a)$$

$$\partial_t \rho + \partial_i(\rho u_i) = 0, \quad (3.1b)$$

where, u_i , F_i are the flow velocity and the total force in the i -th direction. For the liquid slip flow between two confined parallel plates in figure 1 of interest in our work, $i(j)$ represents the streamwise (x -) or spanwise (y -) direction. Considering the net F-S interaction force from the two solid walls plus an external body force driving the liquid flow, a total force of $\mathbf{F} = \mathbf{F}_s + \rho \mathbf{g}$ (where \mathbf{F} , \mathbf{F}_s and \mathbf{g} are the vector form of F_i , F_s and g), arising in the EFS-LBM scheme (2.2), is exerted on the fluid.

When the liquid flow reaches the steady state and maintains a laminar regime, $\partial_t \rho = 0$, $\partial_t(\rho u_i) = 0$, and the inertial term in the momentum equation (3.1a) is neglected. The lateral flow is stagnant, but the fluid density may vary with the distance from the solid wall due to the F-S interaction force. There is no external body force and only the pressure gradient term is left. So (3.1a) can be rewritten as

$$\partial_y p = 0. \quad (3.2)$$

For the homogeneous gap size of the flow channel (see figure 1), the flow velocity and the fluid density keep unchanged in the streamwise direction. There is no pressure gradient and only an external body force is applied. So (3.1a) is reduced to

$$\rho(y)g + \nu \partial_y [\rho(y) \partial_y u] = 0. \quad (3.3)$$

The continuity equation (3.1b) is satisfied for a control volume at the steady state. Integrating (3.1b) over the gap leads to $\partial_t (\int_0^R \rho(y) dy) = 0$, which means that, $\int_0^R \rho(y) dy$ keeps constant with time. With the specified homogeneous fluid density (ρ_0) at the initial time, the macroscale mass balance equation is obtained

$$\int_0^R \rho(y) dy = \rho_0 R. \quad (3.4)$$

The no-slip boundary condition at solid surface and the maximum velocity in the middle of the gap can also be applied, that is,

$$u(0) = 0, \partial_y u(R) = 0. \quad (3.5)$$

From the governing equations and necessary conditions (3.2), (3.3), (3.4) and (3.5), the analytical solutions of density and velocity profiles, slip length and permeability ratio for the liquid slip flow between two confined parallel plates (see figure 1) can be derived.

3.1. Density and velocity profiles

Substituting the macroscale fluid pressure equation (2.9a, b) with the mesoscale F-S interaction force considered into (3.2) gives

$$\partial_y \rho - \frac{g_s}{c_s^2} \rho(y) \left[\exp\left(-\frac{y}{\eta}\right) - \exp\left(-\frac{2R-y}{\eta}\right) \right] = 0, \quad (3.6a)$$

$$\partial_y \rho - \frac{g_s}{c_s^2} \rho(y) \left[\frac{1}{y^n} - \frac{1}{(2R-y)^n} \right] = 0. \quad (3.6b)$$

Let's specify $a = g_s/c_s^2$, which refers to the interaction strength in the following unless stated otherwise. (3.6a, b) can be rewritten as

$$\frac{\partial_y \rho}{\rho(y)} = a \left[\exp\left(-\frac{y}{\eta}\right) - \exp\left(-\frac{2R-y}{\eta}\right) \right], \quad (3.7a)$$

$$\frac{\partial_y \rho}{\rho(y)} = a \left[\frac{1}{y^n} - \frac{1}{(2R-y)^n} \right]. \quad (3.7b)$$

By solving the first-order homogeneous ordinary differential equations about the fluid density (3.7a, b) with the aid of auxiliary condition (3.4), the analytical solution of density profile based on EXF and PLF force functions, respectively, can be obtained as below

$$\rho(y) = \rho_0 A_1 \exp[-aw_1(y)], \quad (3.8a)$$

$$\rho(y) = \rho_0 A_2 \exp[-aw_2(y)], \quad (3.8b)$$

where,

$$w_1(y) = \eta \left[\exp\left(-\frac{y}{\eta}\right) + \exp\left(-\frac{2R-y}{\eta}\right) \right], A_1 = \frac{R}{\int_0^R \exp[-aw_1(y)] dy},$$

$$w_2(y) = \frac{1}{n-1} \left[\frac{1}{y^{n-1}} + \frac{1}{(2R-y)^{n-1}} \right], A_2 = \frac{R}{\int_0^R \exp[-aw_2(y)] dy}.$$

Rearranging (3.3) leads to the following formulation

$$\partial_y^2 u + \frac{\partial_y \rho}{\rho(y)} \partial_y u = -b, \quad (3.9)$$

where, $b = g/\nu$ (with the constant value of ν) represents the magnitude of external body force in the following unless stated otherwise. (3.9) provides the second-order nonhomogeneous ordinary differential equations about the flow velocity. By applying equation (3.5), the analytical solutions of velocity profile based on EXF and PLF force functions, respectively, can be derived as

$$u(y) = b \int_0^y \exp[aw_1(r)] \int_r^R \exp[-aw_1(s)] ds dr, \quad (3.10a)$$

$$u(y) = b \int_0^y \exp[aw_2(r)] \int_r^R \exp[-aw_2(s)] ds dr. \quad (3.10b)$$

3.2. Slip length and permeability ratio

In order to obtain the slip length, (3.10a, b) should be transformed into the same form as (2.12) for the bulk velocity profile. Reformulating (3.10a, b) as

$$u(y) = \frac{b}{2} q_m(y) \quad (m = 1, 2), \quad (3.11)$$

where,

$$q_1(y) = 2 \int_0^y \exp[aw_1(r)] \int_r^R \exp[-aw_1(s)] ds dr,$$

$$q_2(y) = 2 \int_0^y \exp[aw_2(r)] \int_r^R \exp[-aw_2(s)] ds dr.$$

The expression of $q_m(y)$ can be approximated by a second-order Taylor series expansion around the middle of the gap ($y \approx R$). Then (3.11) is rearranged as

$$u(y)|_{y \approx R} \cong \frac{b}{2} \left[\frac{q_m(R)}{0!} + \frac{\partial_y [q_m(R)]}{1!} (y - R) + \frac{\partial_y^2 [q_m(R)]}{2!} (y - R)^2 \right] \quad (m = 1, 2). \quad (3.12)$$

The function and partial derivatives of $q_m(x)$ at $x = R$ can be evaluated as below

$$q_m(R) = q_m(R), \partial_y [q_m(R)] = 0, \partial_y^2 [q_m(R)] = -2 \quad (m = 1, 2). \quad (3.13)$$

Then substituting the computed Taylor coefficients into (3.12) produces

$$u(y)|_{y \approx R} \cong \frac{b}{2} [-y^2 + 2Ry + q_m(R) - R^2] \quad (m = 1, 2). \quad (3.14)$$

By comparing (3.14) with (2.12), a quadratic equation with the unknown slip length is given as follows

$$\lambda^2 + 2R\lambda + R^2 - q_m(R) = 0 \quad (m = 1, 2). \quad (3.15)$$

Then the analytical solution of slip length (normalized by the gap between two flat walls) can be derived as

$$\frac{\lambda}{R} = \frac{1}{R} \sqrt{q_m(R)} - 1 \quad (m = 1, 2). \quad (3.16)$$

Substituting the expressions of $q_m(R)$ into (3.16) gives the analytical normalized slip length based on EXF and PLF force functions, respectively,

$$\frac{\lambda}{R} = \frac{1}{R} \sqrt{2 \int_0^R \exp[aw_1(r)] \int_r^R \exp[-aw_1(s)] ds dr} - 1, \quad (3.17a)$$

$$\frac{\lambda}{R} = \frac{1}{R} \sqrt{2 \int_0^R \exp[aw_2(r)] \int_r^R \exp[-aw_2(s)] ds dr} - 1. \quad (3.17b)$$

The volumetric flux and the mass flux can be calculated based on the analytical profiles of density and velocity. As given by (2.13), the volumetric permeability ratio (k_{rav}) and the mass permeability ratio (k_{ram}) are expressed by

$$k_{rav} = \frac{\int_0^R u(y) dy}{\int_0^R u^*(y) dy}; \quad k_{ram} = \frac{\int_0^R \rho(y) u(y) dy}{\int_0^R \rho_0 u^*(y) dy}. \quad (3.18)$$

Substituting the Poiseuille-type velocity profile (2.11) and the slip velocity profile (3.10a, b) into (3.18) produces the volumetric permeability ratios based on EXF and PLF force functions, respectively,

$$k_{rav} = \frac{3}{R^3} \int_0^R \int_0^y \exp[aw_1(r)] \int_r^R \exp[-aw_1(s)] ds dr dy, \quad (3.19a)$$

$$k_{rav} = \frac{3}{R^3} \int_0^R \int_0^y \exp[aw_2(r)] \int_r^R \exp[-aw_2(s)] ds dr dy. \quad (3.19b)$$

Similarly, the mass permeability ratios based on EXF and PLF force functions, respectively, are derived as

$$k_{ram} = \frac{3A_1}{R^3} \int_0^R \exp[-aw_1(y)] \int_0^y \exp[aw_1(r)] \int_r^R \exp[-aw_1(s)] ds dr dy, \quad (3.20a)$$

$$k_{ram} = \frac{3A_2}{R^3} \int_0^R \exp[-aw_2(y)] \int_0^y \exp[aw_2(r)] \int_r^R \exp[-aw_2(s)] ds dr dy. \quad (3.20b)$$

The analytical solutions (3.8a, b), (3.10a, b), (3.17a, b), (3.19a, b) and (3.20a, b) are derived based on the macroscopic fluid pressure equation (2.9a, b) with the two continuous force functions considered and the macroscopic NS equation (3.1a, b) recovered from the lattice Boltzmann equation. They directly link the macroscale density and velocity profiles, normalized slip length and volumetric and mass permeability ratios with the mesoscale F-S interaction parameters and the gap size of flow channel.

These analytical solutions contain single, double and triple integrals, which can be numerically solved using MATLAB functions. The EXF function is infinitely differentiable, and thus the analytical solutions based on EXF force functions are numerically solvable for arbitrary values of a , η and R . On the other hand, the PLF function has undesirable singularities at $y = 0$ ($2R$) which remain in the analytical solutions, but the numerical solvability of treated analytical solutions based on PLF force function can be maintained for a broad range of a , n and R .

4. Results and discussions

4.1. Validations of analytical profiles of density and velocity

Each of the analytical solutions derived based on EXF and PLF force functions (2.7a, b) has two free interaction parameters. The density ratio profile with respect to these interaction parameters is presented in figure 2. With a larger $|a|$ and a larger η (smaller n) indicating a stronger interaction and a longer interaction range, the density ratio deviates further from one, implying stronger vaporization (or condensation) effect. The density ratio can even reach as high as 10^4 and as low as 10^{-8} . However, the ranges of a and $\eta(n)$ are not arbitrary and should be physically consistent with the observed density ratio of film fluid to bulk fluid, as summarized in table 1, namely,

$$0.1 < \rho_{ra} < 2.0. \quad (4.1)$$

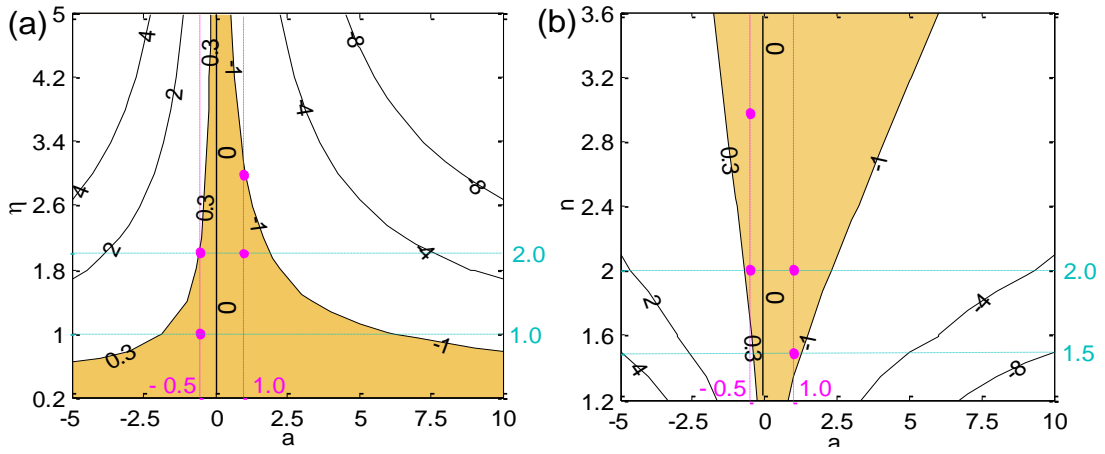


FIGURE. 2. The profiles of density ratio $\log_{10}(\rho_{ra})$ with respect to interaction parameters a and $\eta(n)$ in EXF (a) and PLF (b) force functions, respectively, for the gap size of $R = 100$ lu. The shaded region is the range of a and $\eta(n)$ where the value of ρ_{ra} is between 0.1 and 2.0 as observed in various experimental investigations (see table 1). The eight solid circles represent the values of a and $\eta(n)$ used for comparing analytical solutions with LBM solutions. $\eta = 1.0, 2.0$ and $n = 1.5, 2.0$ are used for investigating the analytical solutions that depend on a . All the variables are presented in lattice units (the same holds for the following figures unless stated otherwise).

The shaded region in figure 2 shows the ranges of a and $\eta(n)$ of the two force functions satisfying the observed range of density ratio. Following this guideline, the reasonable range of a becomes very limited for the large η (small n) and very broad for the small η (large n).

With the values of a and $\eta(n)$ taken from the shaded range (see figure 2), the analytical solutions of density profiles (3.8a, b) and velocity profiles (3.10a, b) are plotted in figure 3. For the same $|a|$ but a larger η (smaller n), the film and bulk fluid densities are further away from the initial density, and the maximum velocities deviate more significantly from that in the no-slip flow. Note that, the bulk fluid density profile based on PLF force function is not as flat as that based on EXF force function.

The analytical solutions based on the two force functions are in an excellent agreement with the numerical solutions using the EFS-LBM scheme, respectively (see figure 3). Thus the analytical solutions (3.8a, b) and (3.10a, b) numerically solved by MATLAB functions are well validated. They can provide benchmark solutions of liquid slip flow for various advanced LBM schemes and experimental investigations.

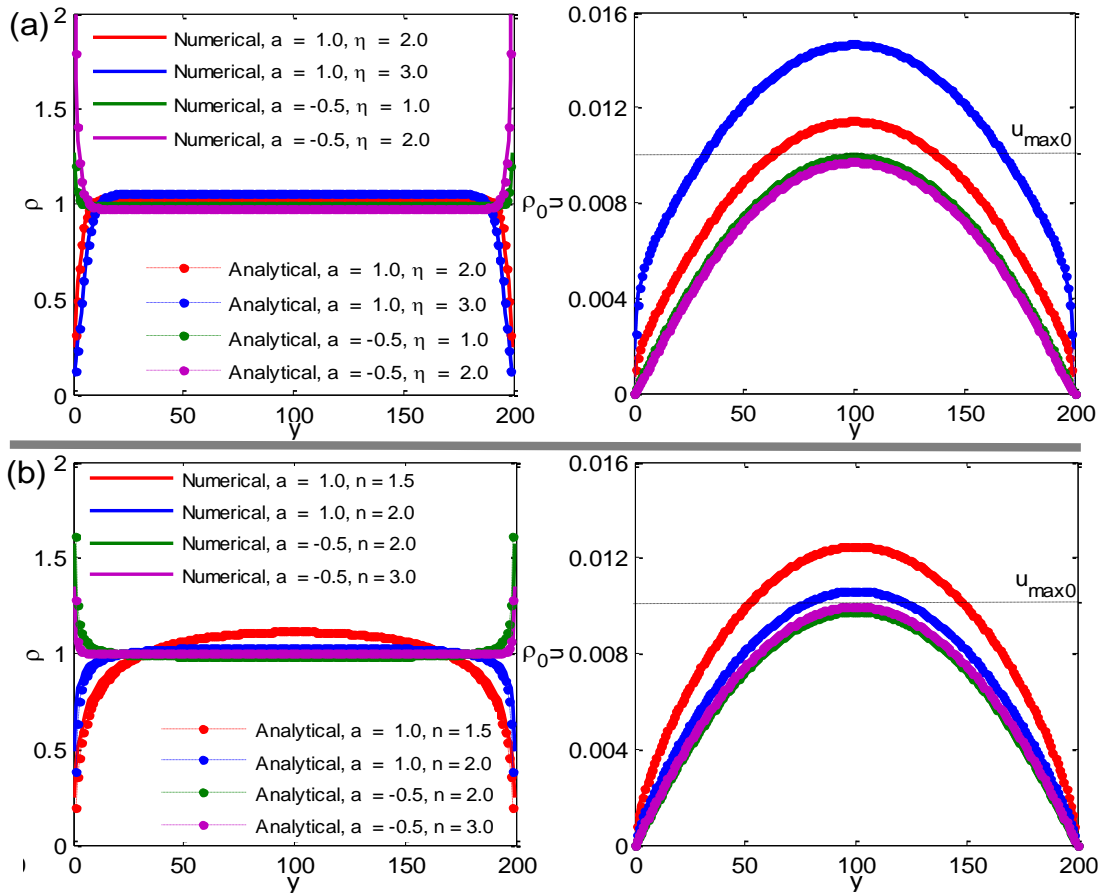


FIGURE. 3. Comparison of numerical and analytical solutions of density and velocity profiles based on EXF (a) and PLF (b) force functions, respectively. ρ_0 is the specified homogeneous fluid density at the initial time. $u_{\max 0}$ is the maximum velocity in the middle of the gap under the no-slip boundary condition.

4.2. Implications of analytical slip length and permeability ratio

In the engineering context, such as, oil in shale matrix (Afsharpoor & Javadpour, 2016) and water in tight sandstone reservoir (Cheng *et al.*, 2017), the slip length and the permeability ratio are always used to quantify the degree of liquid slip flow through the tight porous media, which is controlled by the physicochemical property of solid surface and the gap size of flow channel. As shown in figure 4, within the reasonable range of interaction strength (see figure 2), the normalized slip length (3.17a, b) and the volumetric and mass permeability ratios (3.19a, b) and (3.20a, b) increases more than proportionally with a for $\eta = 1.0, 2.0$ and $n = 1.5, 2.0$, respectively, and the curves of normalized slip length and volumetric and mass permeability ratios are steeper for $\eta = 2.0$ ($n = 1.5$) than those for $\eta = 1.0$ ($n = 2.0$), implying a more significant F-S interaction effect on the flow properties. The analytical volumetric permeability ratios based on the two force functions cover the measured range of flow enhancement ratio (Schnell, 1956; Churaev *et al.*, 1984).

It is interesting to find another two facts in figure 4. (1) Within the physically consistent range of density ratio, the normalized slip length and the volumetric and mass permeability ratios based on EXF force function cover a broader range than those based on PLF force function. (2) The volumetric and mass permeability ratio curves based on EXF force function almost collapse, while the mass permeability ratio curve based on PLF force function is a bit steeper than the volumetric permeability ratio curve. These two facts manifest the different behaviours of film fluid density and bulk fluid density profile based on the two force functions.

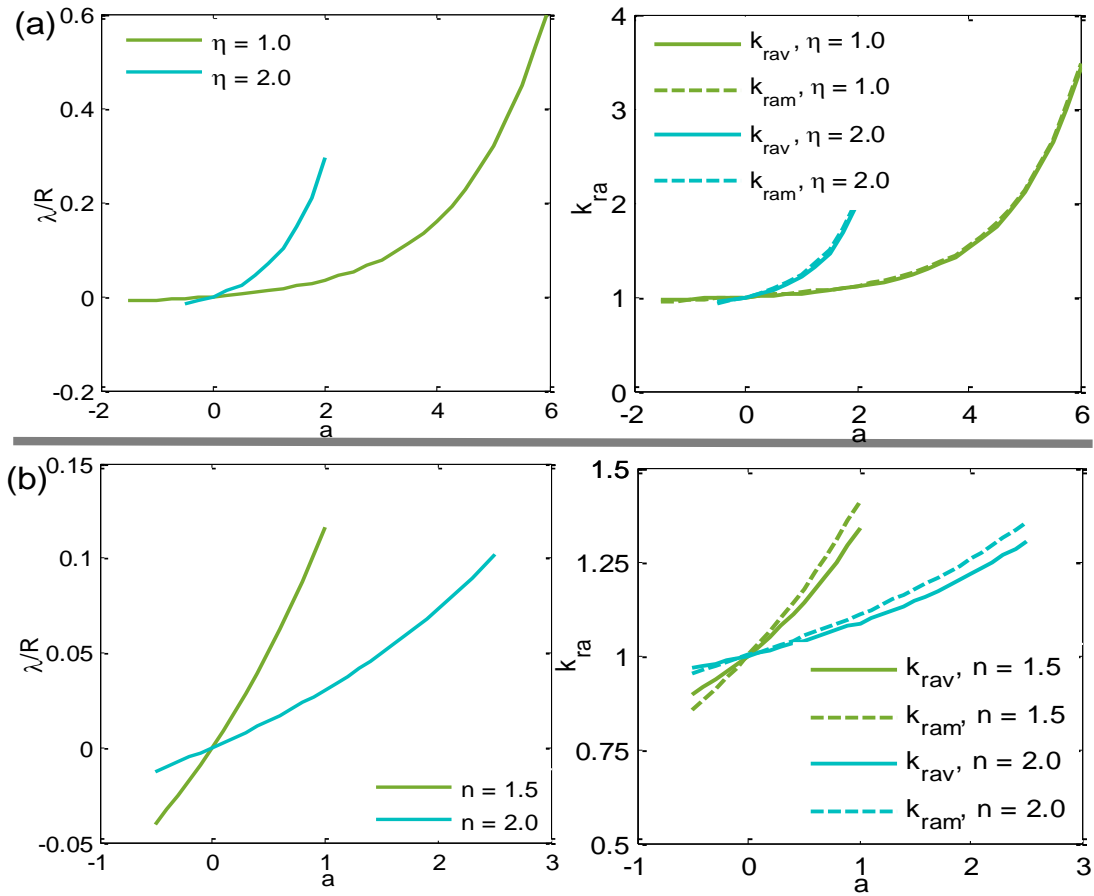


FIGURE. 4. The normalized slip length and the permeability ratio as functions of interaction strength based on EXF (a) and PLF (b) force functions, respectively, for the gap size of $R = 100$ lu.

The slip length and the volumetric permeability ratio can be directly correlated at the macroscale. If neglecting the effect of near-wall velocity on the volumetric flux, substituting the no-slip velocity profile (2.11) and the approximated bulk velocity profile (2.12) into (3.18) can estimate the volumetric permeability ratio, such as (Li *et al.*, 2018a),

$$k_{\text{rav}} = \begin{cases} 1 + 3 \left(\frac{\lambda}{R} + \frac{\lambda^2}{2R^2} \right), & \lambda > 0, \\ \left(1 + \frac{\lambda}{R} \right)^3, & \lambda < 0. \end{cases} \quad (4.2)$$

The estimated volumetric permeability ratio (4.2) as a function of the normalized slip length is illustrated in figure 5, and they pose a positive correlated relationship.

If reorganizing the analytical data shown in figure 4, the analytical volumetric permeability ratio versus normalized slip length curve can be obtained (see figure 5). An excellent consistency between the estimated and analytical volumetric permeability ratios based on EXF force function can be found, whereas the analytical volumetric permeability ratio based on PLF force function tends to deviate from the estimated one when $|\lambda|/R$ increases (the F-S interaction effect strengthens). These results reflect the different near-wall velocity profiles resulted from the two force functions.

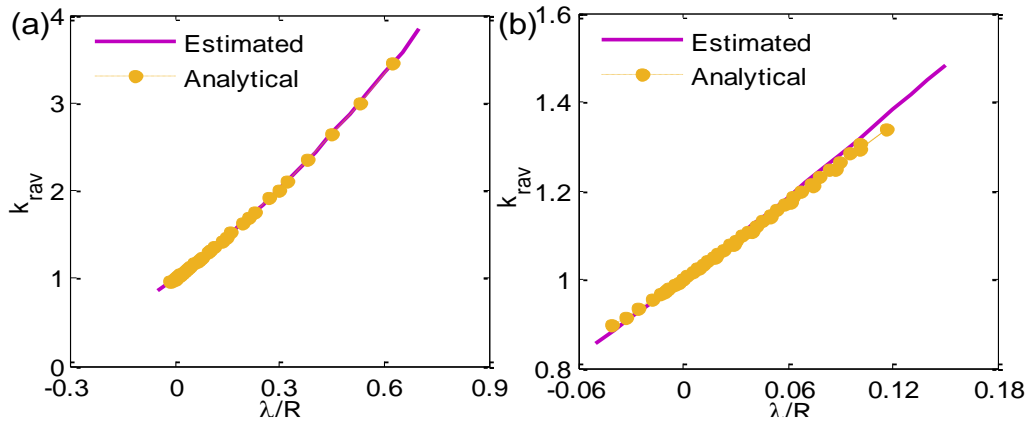


FIGURE 5. Comparison of the estimated volumetric permeability ratio (4.2) and the analytical volumetric permeability ratios (3.19a, b) as a function of the normalized slip length (3.17a, b) based on EXF (a) and PLF (b) force functions, respectively.

As presented in figure 6, the normalized slip lengths $|\lambda|/R$ (for convenience in evaluating the slip flow effect on the macroscopic flow properties) based on the two force functions increase rapidly with the decreased gap of the parallell-plate channel for each pair of a and $\eta(n)$, that is

$$\frac{d(|\lambda|/R)}{dR} < 0. \quad (4.3)$$

Also, the volumetric and mass permeability ratios increase (decrease) nonlinearly with the narrowed gap for $a > 0$ ($a < 0$). These results are consistent with the observation that the F-S interaction effect (liquid slip flow) is quite important to the tight porous media (Afsharpoor & Javadpour, 2016; Cheng *et al.*, 2017).

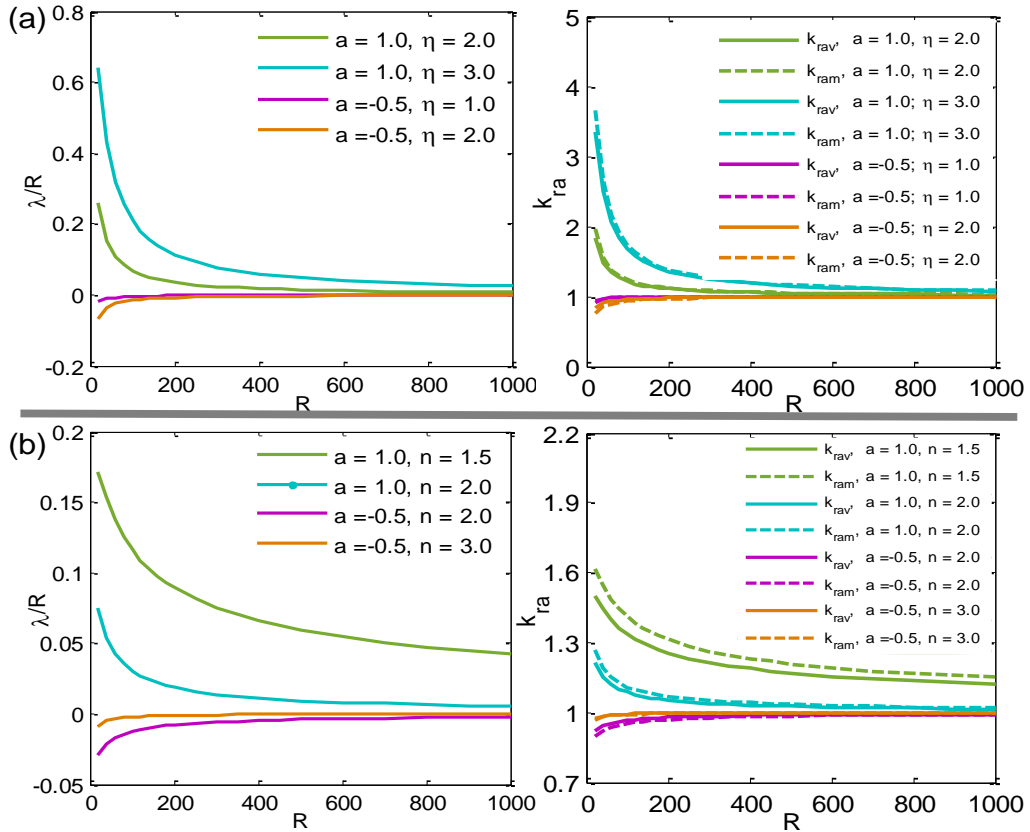


FIGURE 6. The normalized slip length and the permeability ratio as functions of the gap size of the parallell-plate channel based on EXF (a) and PLF (b) force functions, respectively.

It is worthwhile to note (see figure 6) that, the deviation between the volumetric permeability ratio and the mass permeability ratios based on PLF force function is greater than that based on EXF force function. As the gap increases, the normalized slip length and the permeability ratios based on EXF force function tend to converge rapidly to zero and one, respectively, while the normalized slip length and the permeability ratios based on PLF force function tend to converge much slowly to zero and one, respectively. These findings indicate the different behaviours of bulk fluid density profile and flow velocity profile based on the two force functions.

When the gap is narrower than a critical size (R_0) (see figure 7), however, the normalized slip length $|\lambda|/R$ based on EXF force function decreases rapidly with the narrowed gap for arbitrary values of η , and a similar trend of $|\lambda|/R$ based on PLF force function is also found for $n \geq 1.2$. These results imply a weakening liquid slip flow in tight porous media with the narrowed gap, and are inconsistent with the physical realities (Afsharpoor & Javadpour, 2016; Cheng *et al.*, 2017). As discussed in §2.2, the extremely narrow gap results in a high Kn ($\text{Kn} > 0.1$) where the mesoscopic LBM model will fail. Another physically inconsistent result in figure 7 is that, $|\lambda|/R$ based on PLF force function always decreases with the decreased gap for $n < 1.2$.

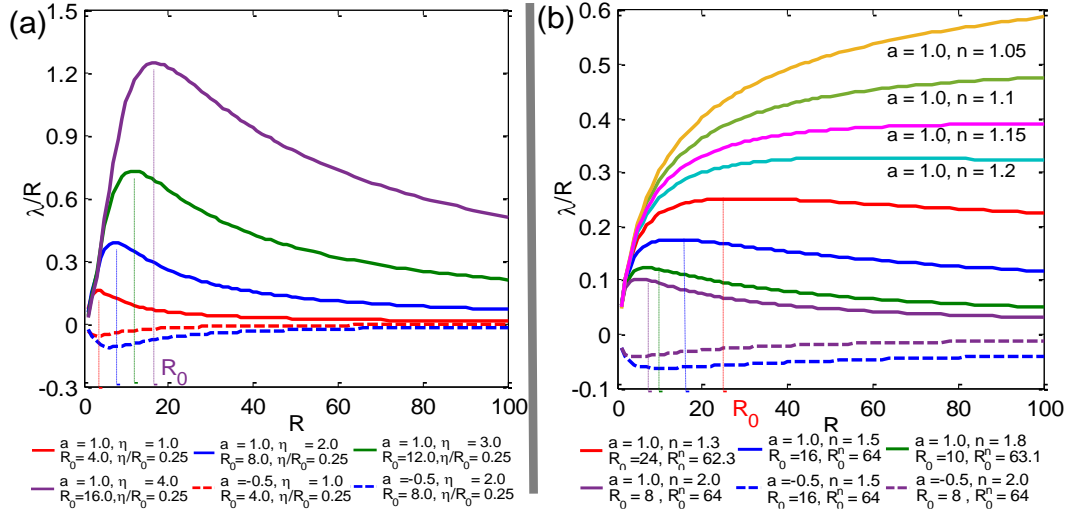


FIGURE. 7. The normalized slip length as functions of the gap size of the parallel-plate channel based on EXF (a) and PLF (b) force functions, respectively. As shown under each subfigure, the critical gap size R_0 for each set of interaction parameters of the two force functions are calculated based on the criteria in (4.3). The relations of $\eta/R_0 = 0.25$ and $R_0^n = 64$ can be found for EXF and PLF force functions, respectively.

To avoid these undesirable cases, the gap size of investigation should obey $R > R_0$. The critical gap sizes for the two force functions can be obtained in figure 7, as below

$$R_0 = \eta/0.25, \quad (4.4a)$$

$$R_0 = 64^{1/n}. \quad (4.4b)$$

Moreover, $n \geq 1.2$ should be kept for the PLF force function. Therefore, to keep a consistency with the increasing trend of permeability ratio with narrowed pore size (Afsharpoor & Javadpour, 2016; Cheng *et al.*, 2017), the values of interaction parameters η and n in EXF and PLF force functions should follow

$$\eta < 0.25R, \quad (4.5a)$$

$$n > \max[1.2, \log_R 64]. \quad (4.5b)$$

(4.1) and (4.5a, b) provide useful guidelines of the reasonable range of interaction parameters, a and $\eta(n)$, when our derived mesoscale analytical solutions are used in experimental investigations.

4.3. Applications in a benchmark slip flow

A benchmark water slip flow experiment (Tretheway & Meinhart, 2002) was carried out in a rectangular duct (see figure 8(a)). The directions of length, width and depth are denoted as x , y and z coordinates, respectively, and the dimension is $8.25\text{cm} \times 300\mu\text{m} \times 30\mu\text{m}$. The four solid walls (α_1 , α_2 , β_1 and β_2) in the flow direction are uniformly hydrophilic or hydrophobic. The clean glass surface is naturally hydrophilic, while it becomes hydrophobic when covered with an octadecyltrichlorosilane (OTS) layer. The deionized water is injected into the microchannel at a constant flux using a syringe pump. The velocity profile measured at $z = 15\mu\text{m}$ near solid surface using micron-particle image velocimetry (μ -PIV) has been used for validating the mesoscopic LBM model based on the interaction force function at the particle level (Li *et al.*, 2018a), which is different from that between fluid particle and flat wall proposed in this study.

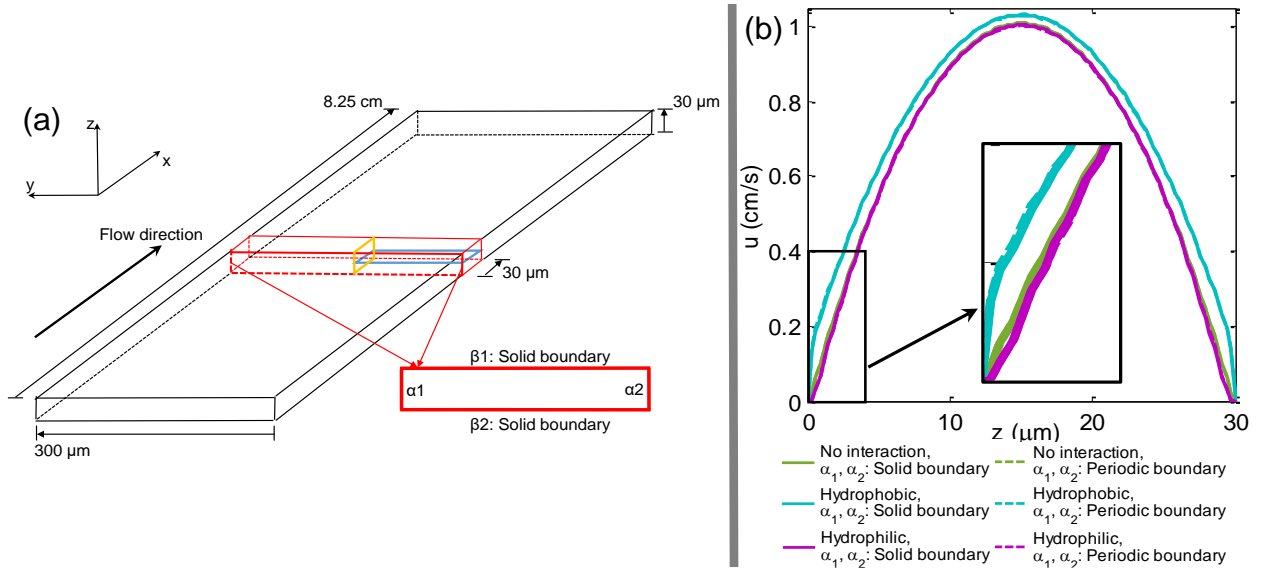


FIGURE. 8. (a) Dimension of the rectangular duct in the slip flow experiment (Tretheway & Meinhart, 2002) (black cube) and in the LBM simulation (Li *et al.*, 2018a) (red cube), respectively. Blue rectangle ($z = 15\mu\text{m}$) and yellow rectangle ($y = 150\mu\text{m}$) are the planes of investigation in those work and in this study, respectively. Red rectangle represents the cross section of the microchannel. The top and bottom walls, β_1 and β_2 , are solid boundaries (where both the no-slip boundary condition and the F-S interaction force are applied), and the left and right walls, α_1 and α_2 , are solid or periodic boundaries. (b) Comparison of the simulated velocity profiles using the validated LBM model (Li *et al.*, 2018a) when α_1 and α_2 are solid and periodic boundaries, respectively.

An attempt is made in this section to apply our proposed analytical solutions for the parallel-plate microchannel to the aforementioned slip flow experiment. Considering the aspect ratio of the cross section of the flow channel is $300\mu\text{m} : 30\mu\text{m} = 10 : 1$, the velocity profile of interest here is located at $y = 150\mu\text{m}$ over the vertical direction (see figure 8(a)). This velocity profile is controlled by the top and bottom walls (β_1 and β_2) with a narrower gap. Moreover, the effect of the left and right walls (α_1 and α_2) should be evaluated to check if the analytical solutions are applicable to the rectangular duct used in the flow experiment.

The velocity profile over the vertical direction (see figure 8(a)) was not measured in the flow experiment (Tretheway & Meinhart, 2002), but it can be obtained from the numerical simulations using the validated LBM model (Li *et al.*, 2018a). β_1 and β_2 walls are always solid boundaries, while α_1 and α_2 walls can be eliminated by being set up as periodic boundaries. Figure 8(b) illustrates that, there is almost no difference in the velocity profiles for hydrophilic, hydrophobic and no-interaction solid surfaces, when α_1 and α_2 are solid boundaries and periodic ones. It shows that, the rectangular duct in the flow experiment can be simplified as a parallel-plate microchannel in terms of the velocity profile over the vertical direction, where our analytical solutions can be applied accordingly.

In our analytical method, $2R = 600$ lu, $\nu = 3.0$ lu²/ts and $\rho_0 = 1.0$ mu/lu³ are used to represent the gap size of the flow channel (30μm), kinematic viscosity of water (1.5×10^{-6} m²/s) and water density (1.0×10^3 kg/m³), respectively. As illustrated in figure 9, by fitting the analytical velocity profiles based on the two proposed force functions to the simulated velocity profile over the vertical direction, the interaction parameters a and $\eta(n)$ can be obtained.

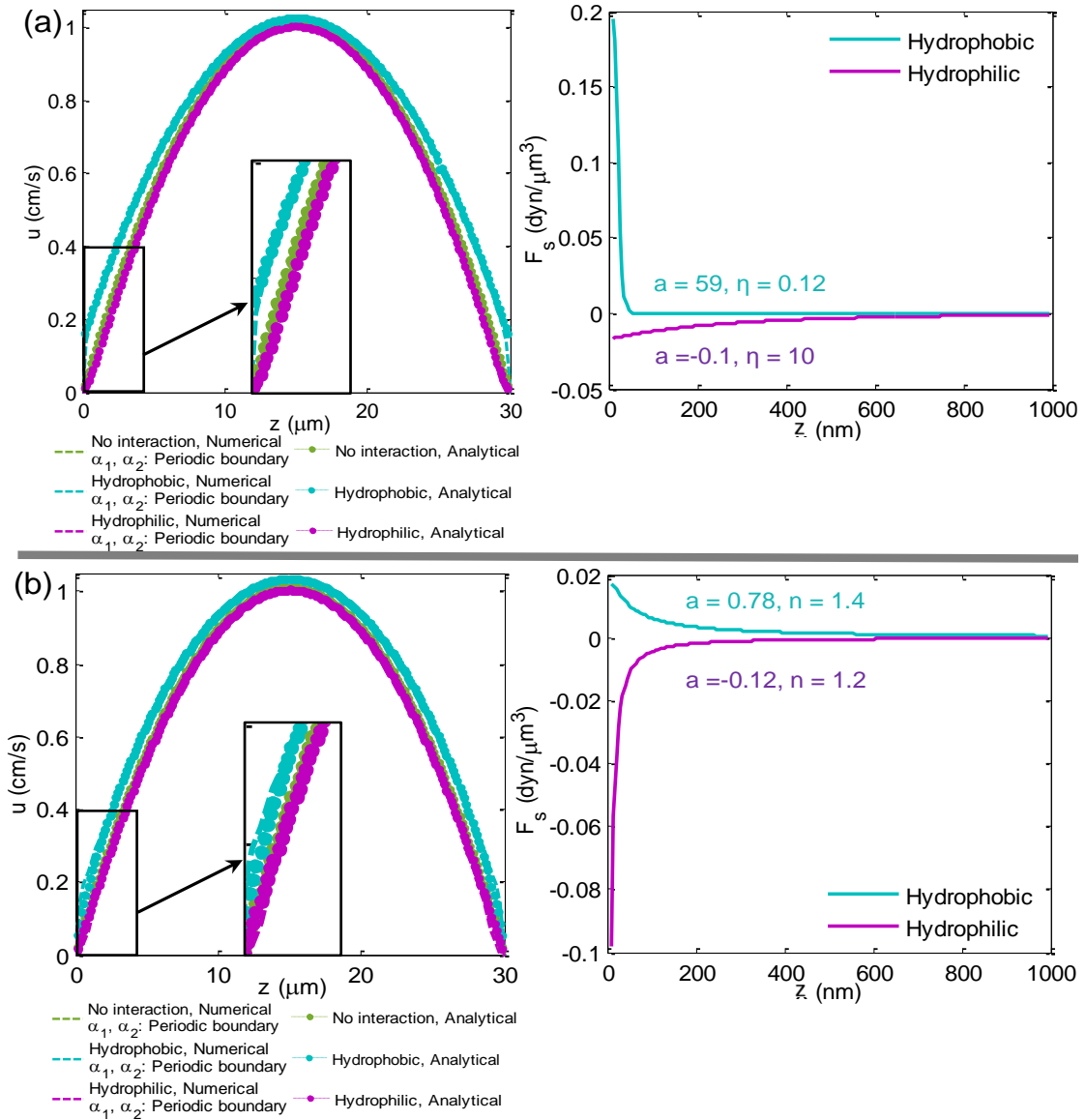


FIGURE. 9. Comparison of the simulated and analytical velocity profiles (the simulated profile is obtained from the validated LBM model (Li *et al.*, 2018a), and the recovered F-S interaction force curves based on EXF (a) and PLF (b) force functions, respectively.

The slip lengths based on EXF and PLF force functions are calculated as $1.16\mu\text{m}$ and $1.22\mu\text{m}$, respectively, for hydrophobic surface, which are consistent with the slip length of around $1\mu\text{m}$ as estimated in (Tretheway & Meinhart, 2002; Li *et al.*, 2018a). For hydrophilic surface, the negative slip lengths are calculated as $-0.37\mu\text{m}$ and $-0.30\mu\text{m}$, respectively, which were noticed but not quantified in (Zhu *et al.*, 2005; Li *et al.*, 2018a). The density ratios based on EXF and PLF force functions are 0.998 and 0.182, respectively, for hydrophobic surface, and they are 2.47 and 1.47, respectively, for hydrophilic surface. These density ratios are roughly within the physically reasonable range in (4.1). The EXF and PLF force functions produce different density ratios with the same velocity profile on hydrophobic or hydrophilic surface matched, implying different film fluid density behaviors based on the two force functions. It is an open question whether the EXF or PLF function is more practical, because accurate observations of density profile near solid surface and density ratio for validating the interaction force functions are still unavailable.

The recovered force curves (2.7a, b) of the two force functions with the density profile included are also plotted in figure 9. To match the same velocity profile (F-S interaction effect) on hydrophobic surface, EXF force curve has a shorter interaction distance but a larger interaction strength, while PLF force curve has a weaker interaction strength but a longer interaction distance. Similar findings can also be obtained on hydrophilic surface. The recovered F-S force curve can be used to predict the slip flow for the given fluid and solid surface with different gap sizes.

5. Conclusions

In this paper, the continuous exponentially and power law decaying force functions are proposed for describing the physics of F-S interaction force in the LBM model framework, which is responsible for the liquid slip flow with Kn in the range of 0.001–0.1. Both the macroscopic fluid pressure equation with the mesoscale F-S interaction considered and the macroscopic NS equation recovered from the lattice Boltzmann equation are used to derive the analytical solutions. To the best of authors' knowledge, it is the first time to provide the analytical solutions of density and velocity profiles, slip length and permeability ratio for the liquid slip flow between two confined parallel plates.

The analytical solutions with the single (multiple) integral included are numerically solvable using MATLAB functions, and are well validated by the LBM solutions. The values of F-S interaction parameters are not arbitrary. The physically reasonable ranges are determined by the observed range of density ratio (such as, $0.1 < \rho_{\text{ra}} < 2.0$), and the increasing permeability ratio with the narrowing gap size (leading to $\eta < 0.25R$ and $n > \max[1.2, \log_R 64]$). The different decaying nature of the two force functions can be manifested by the different behaviours of film fluid density, bulk fluid density profile, and near-wall and bulk flow velocity profiles.

An application of analytical solutions to a benchmark slip flow experiment (Tretheway & Meinhart, 2002) is carried out, where the rectangular duct can be simplified as a parallel-plate microchannel in terms of the velocity profile over the vertical direction. By fitting the velocity profile obtained from the validated LBM model (Li *et al.*, 2018a), the continuous F-S interaction force curves with two free interaction parameters were calibrated. The verification of our analytical model with the calibrated interaction force curves using the available flow data for the same pair of solid surface and liquid should be performed to further validate our proposed model.

The analytical solutions derived based on the two continuous force functions relate the macroscale flow properties with the mesoscale F-S interaction parameters and the gap size of flow channel. They uncover the physical mechanism of the liquid slip flow in microfluidic devices and tight porous media, and provide useful implications in the engineering context. In the future, we will validate which form of interaction force function is closer to the given solid surface using the available flow data.

References

- Afsharpoor, A., & Javadpour, F., 2016. Liquid slip flow in a network of shale noncircular nanopores. *Fuel* **180**, 580–590.
- Anderson, D. M., & Low, P. F., 1957. Density of water adsorbed on Wyoming bentonite. *Nature* **180**, 1194.
- Baudry, J., Charlaix, E., Tonck, A., & Mazuyer, D., 2001. Experimental evidence for a large slip effect at a nonwetting fluid-solid interface. *Langmuir* **17**, 5232–5236.
- Benzi, R., Biferale, L., Sbragaglia, M., & et al., 2006a. Mesoscopic two-phase model for describing apparent slip in micro-channel flows. *Europhys. Lett.* **74**, 651–657.
- Benzi, R., Biferale, L., Sbragaglia, M., & et al., 2006b. Mesoscopic modeling of a two-phase flow in the presence of boundaries: The contact angle. *Phys. Rev. E* **74**, 021509.
- Benzi, R., Biferale, L., Sbragaglia, M., & et al., 2006c. Mesoscopic modelling of heterogeneous boundary conditions for microchannel flows. *J. Fluid Mech.* **548**, 257–280.
- Bocquet, L., & Charlaix, E., 2010. Nanofluidics: from bulk to interfaces. *Chem. Soc. Rev.* **39**, 1073–1095.
- Cheng, Y., Zhang, C., & Zhu, L. Q., 2017. A fractal irreducible water saturation model for capillary tubes and its application in tight gas reservoir. *J. Petrol. Sci. Eng.* **159**, 731–739.
- Churaev, N. V., Sobolev, V. D., & Somov, A. N., 1984. Slippage of liquids over lyophobic solid surfaces. *J. Colloid Interf. Sci.* **97**, 574–581.
- Craig, V. S. J., Neto, C., & Williams, D. R. M., 2001. Shear-Dependent Boundary Slip in an Aqueous Newtonian Liquid. *Phys. Rev. Lett.* **87**, 54504.
- Davis, M. J., & Lauga, E., 2009. Geometric transition in friction for flow over a bubble mattress. *Phys. Fluids* **21**, 011701.
- Derjaguin, B. V., & Churaev, N. V., 1987. Structure of water in thin layers. *Langmuir* **3**, 607–612.
- Ewing, D. T., & Spurway, C. H., 1930. The density of water adsorbed on silica gel. *J. Am. Chem. Soc.* **52**, 4635–4641.
- Harting, J., Kunert, C., & Herrmann, H. J., 2006. Lattice Boltzmann simulations of apparent slip in hydrophobic microchannels. *Europhys. Lett.* **75**, 328–334.
- Ho, T. A., Papavassiliou, D. V., Lee, L. L., & Striolo, A., 2011. Liquid water can slip on a hydrophilic surface. *P. Natl. Acad. Sci. USA* **108**, 16170.
- Huang, D. M., Sendner, C., Horinek, D., & et al., 2008. Water slippage versus contact angle: A quasiuniversal relationship. *Phys. Rev. Lett.* **101**, 226101.
- Ishida, N., Inoue, T., Miyahara, M., & Higashitani, K., 2000. Nano bubbles on a hydrophobic surface in water observed by tapping-mode atomic force microscopy. *Langmuir* **16**, 6377–6380.
- Joseph, P., & Tabeling, P., 2005. Direct measurement of the apparent slip length. *Phys. Rev. E* **71**, 035303.
- Kulasinski, K., 2016. Effects of water adsorption in hydrophilic polymers. In: *Polymer Science: Research Advances, Practical Applications and Educational Aspects* (Formatex Research Center), 217–223.
- Kunert, C., & Harting, J., 2008. On the effect of surfactant adsorption and viscosity change on apparent slip in hydrophobic microchannels. *Prog. Comput. Fluid Dy.* **8**, 018090.
- Li, Z., Galindo-Torres, S., Scheuermann, A., & Li, L., 2018a. Mesoscopic approach to fluid-solid interaction: Apparent liquid slippage and its effect on permeability estimation. *Phys. Rev. E* **98**, 052803.

- Li, Z., Galindo-Torres, S., Yan, G., & et al., 2018b. A lattice Boltzmann investigation of steady-state fluid distribution, capillary pressure and relative permeability of a porous medium: Effects of fluid and geometrical properties. *Adv. Water Resour.* **116**, 153–166.
- Li, Z., Galindo-Torres, S., Yan, G., & et al., 2019. Pore-scale simulations of simultaneous steady-state two-phase flow dynamics using a lattice Boltzmann model: Interfacial area, capillary pressure and relative permeability. *Transport Porous Med.*, **129**, 295–320.
- Liu, D. X., Yue, X. A., Wang, L. M., & et al., 2006. Model study on the irreducible water saturation by centrifuge experiments. *J. Petrol. Sci. Eng.* **53**, 77–82.
- Martin, R. T., 1962. Adsorbed water on clay: a review. In: *Clays and Clay Minerals: Proceedings of the Ninth National Conference* (Pergamon Press), 28–70.
- Martini, A. Roxin, R. Q. Snurr, & et al., 2008. Molecular mechanisms of liquid slip. *J. Fluid Mech.* **600**, 257–269.
- Olodovskii, P. P., 1967. Adsorbed water density distribution in disperse media. *J. Eng. Phys.* **12**, 263–266.
- Olodovskii, P.P., 1981. Density of adsorbed water in disperse systems. *J. Eng. Phys.* **40**, 433–438.
- Porter, M. L., Coon, E. T., Kang, Q., & et al., 2012. Multicomponent interparticle-potential lattice Boltzmann model for fluids with large viscosity ratios. *Phys. Rev. E* **86**, 036701.
- Richardson, S., 1973. On the no-slip boundary condition. *J. Fluid Mech.* **59**, 707–719.
- Roy, S., Raju, R., Chuang, H. F., & et al., 2003. Modeling gas flow through microchannels and nanopores. *J. Appl. Phys.* **93**, 4870–4879.
- Ruckenstein, E., & Rajora, P., 1983. On the no-slip boundary condition of hydrodynamics. *J. Colloid Interf. Sci.* **96**, 488–491.
- Sbragaglia, M. & Succi, S., 2005. Analytical calculation of slip flow in lattice Boltzmann models with kinetic boundary conditions. *Phys. Fluids* **17**, 093602.
- Schnell, E., 1956. Slippage of Water over Nonwetttable Surfaces. *J. Appl. Phys.* **27**, 1149–1152.
- Succi, S., 2001. *The lattice Boltzmann equation: for fluid dynamics and beyond*. Oxford university press.
- Succi, S., 2002. Mesoscopic Modeling of Slip Motion at Fluid-Solid Interfaces with Heterogeneous Catalysis. *Phys. Rev. Lett.* **89**, 064502.
- Tang, G. H., Tao, W. Q., & He, Y. L., 2004. Lattice Boltzmann method for simulating gas flow in microchannels. *Int. J. Mod. Phys. C* **15**, 335–347.
- Tang, G. H., Tao, W. Q., & He, Y. L., 2005. Lattice Boltzmann method for gaseous microflows using kinetic theory boundary conditions. *Phys. Fluids* **17**, 058101.
- Tretheway, D. C., & Meinhart, C. D., 2002. Apparent fluid slip at hydrophobic microchannel walls. *Phys. Fluids* **14**, L9.
- Tretheway, D. C., & Meinhart C. D., 2004. A generating mechanism for apparent fluid slip in hydrophobic microchannels. *Phys. Fluids* **16**, 1509–1515.
- Vinogradova, O. I., 1998. Implications of hydrophobic slippage for the dynamic measurements of hydrophobic forces. *Langmuir* **14**, 2827–2837.
- Vinogradova, O. I., 1999. Slippage of water over hydrophobic surfaces. *Int. J. Miner. Process* **56**, 31–60.
- Wu, K., Chen, Z., Li, J., & et al., 2017. Wettability effect on nanoconfined water flow. *P. Natl. Acad. Sci. USA* **114**, 3358–3363.
- Zhang, J., & Kwok, D. Y., 2004. Apparent slip over a solid-liquid interface with a no-slip boundary condition. *Phys. Rev. E* **70**, 56701.
- Zhang, J., Li, B., & Kwok, D. Y., 2004. Mean-field free-energy approach to the lattice Boltzmann method for liquid-vapor and solid-fluid interfaces. *Phys. Rev. E*, **69**, 32602.
- Zhu, L., Tretheway, D., Petzold, L., & Meinhart, C., 2005. Simulation of fluid slip at 3D hydrophobic microchannel walls by the lattice Boltzmann method. *J. Compu. Phys.* **202**, 181–195.